Emission of matter by hypervelocity impact

N. A. Inogamov, A. B. Konstantinov, S. I. Anisimov, and S. B. Zhitenev

L. D. Landau Institute of Theoretical Physics, USSR Academy of Sciences

(Submitted 7 December 1990; resubmitted 14 February 1991)
Zh. Eksp. Teor. Fiz. **99**, 1699–1710 (June 1991)

We investigate the emission accompanying the interaction of fast condensed particles with a target surface, using modern numerical methods and computers. The distributions of the emitted matter in velocity and in energy are computed. The sensitivity of these distributions to the problem parameters is investigated.

1. INTRODUCTION

The traditional interest in the interaction between fast condensed particles and a surface has recently been revived. This interaction engages several large research groups in the USSR and abroad, and is the subject of national and international conferences. The experiments are performed mainly in laboratories under terrestrial conditions, using rather massive strikers, and hence at relatively low impact velocities, $v_0/c_s = 1$–10. Such an impact is usually called high-velocity. We designate hereafter by v_0 the initial striker velocity and by c_s the speed of sound in the target material prior to the impact. Of principal interest in the studies are the the damage to the target, viz., crater formation, plate puncture, and chip and crack formation.

The subject of the material emitted in hypervelocity impact ($v_0/c_s \sim 10^2$) has been little investigated. Only two recent papers can be cited.[1,2] A brief communication[2] reports the use of computer simulation of an emitted plasma flare to calculate the characteristics of powder-impact mass analyzers (Soviet "PUMA" and western "PIA") mounted on board the interplanetary satellites Vega-1 and Vega-2 in their flyby of Venus towards the Halley comet, and on board the Giotto probe. The angular distributions of the plasma behind the accelerating grid are described and attempts are reported to control the asymmetry of these distributions by fluting the target surface. The important question of the structure of the plasma flare, which is the subject of the present article, is not touched upon in Ref. 2.

The revived interest in the impact is due both to the fundamental character of these problems and to the large number of important practical applications. These problems are fundamental because the ensuing mechanical effects, such as interactions between multidimensional shock waves, contact discontinuities, and expansion waves, are far from trivial.

Among the numerous applications we note the very important puncturing of high-voltage vacuum equipment by bombarding with dust particles to produce plasma flares and short-circuit vacuum insulation. These questions are the subject of entire sections in recent books [Ref. 3, Chap. 6 and Ref. 4, Chaps. 4, 6, and 7]. Closely related problems arise also in the analysis of the formation of a plasma flare by electric breakdown.[5]

Generation of fast microparticles by first charging and then accelerating them in a linear Van-der-Graaf accelerator, and experimental investigations of impact phenomena, are described in Refs. 6–9. These accelerators can impart to the dust particles record velocities $v_0 \sim 10^2$ km/s. No investigations were made in these experiments, however, of the ejection geometry and of the velocity distribution of the emitted matter.

Interesting experiments with fast dust were made as parts of the Soviet Vega-1 and Vega-2 missions and the European Space Agency (ESA) Giotto mission to the Halley comet. The success of the dust experiments was one of the main accomplishments of these missions. The dust component that dominated in the mass spectrum was investigated using the PUMA and PIA ionization apparatus, the dust counters SP-1 and SP-2, and the APV-N low-frequency plasma-wave analyzer. Impact produces a flare consisting of the impinging dust particles and the target material, and leaves a crater in the solid target. Starting with a certain critical thickness, spallation damage is produced on the rear side of a target of finite thickness, which becomes an open hole in a thinner one.

The ionization instruments mentioned above operate by gathering the emitted charge due to residual ions generated by impact in the plasma flare. Analysis of the results of these experiments answered some questions concerning this flare. In particular, the rate of flare spreading, as predicted by theory,[2] turned out, to be several times lower than the impact velocity. A study of the craters and holes is of interest for protecting spacecraft against dust streams.[12,14] Useful information of this kind resulted from the "Foton" experiment.[15]

The research mentioned above was mainly into relatively "low" velocities resulting from high-velocity impacts. Hypervelocity impacts have been less investigated. It seems that the most up-to-date theory of target damage by hypervelocity impact has been developed in Refs. 12–15.

We conclude this introduction by noting that in general the problems connected with high-velocity impacts constitute a branch of a certain relatively new scientific area called high-energy-density physics. It deals, in addition to high-velocity impacts, with the action of electron, ion, and laser beams on solid targets and with electric explosion of conductors. These processes turn out to have much in common. From the hydrodynamic point of view, these actions produce in a solid target a region of locally heated matter—a hot spot. The decay and expansion of this region in vacuum produces a unique flare consisting of a rapidly moving part containing the material with the highest values of specific entropy, an approximately self-similar power-law tail, and slowly ejected matter expanding with velocities $\sim c_s$. In the high-energy-density region the average initial energy per particle greatly exceeds the characteristic binding energies

0038-5646/91/060948-07$03.00

of the particles. The self-similar tail is formed when this condition is met.

2. DYNAMICS OF EMISSION-FLARE FORMATION

Hypervelocity impact is accompanied by emission of the striking-particle material and of part of the target material. We are interested in the long-time asymptotic spreading. The asymptotic velocity distribution of the emitted material is described by a distribution function

$$f_{d,p}(v_X, v_Y)=\frac{\partial^2 m}{m_d\,\partial v_X\,\partial v_Y}, \tag{2.1}$$

where m_d is the running mass of the striking particle in g/cm (by target or particle "mass" we mean hereafter the running mass). The distribution function $f_{t,p}$ takes a form similar to (2.1). Here and below the subscripts d and t refer respectively to the particle and the target, and the subscript p refers to planar geometry with coordinates x and y normal and tangential to the surface. The values of m in the expressions for the distribution functions $f_{d,p}$ and $f_{t,p}$ refer to the particle and the target, respectively. The distribution (2.1) is obtained in the limit as $t\to\infty$ from the current distributions $f(\mathbf{v}, t)$. The initial distribution functions are equal to

$$f_d(\mathbf{v}, 0(=\delta(\mathbf{v}-\mathbf{v}_0),\quad f_t=(M_t/m_d)\delta(\mathbf{v}),$$

where M_t is the target mass.[1)]

To understand the principles underlying the formation of $f(\mathbf{v})$, we consider the dynamics of the interaction between the particle and the target. Let the z axis pass through the particle-mass center and be perpendicular to the target surface. Consider the aggregate of Lagrangian particles located at $t = 0$ on the z axis. We choose the Lagrangian coordinates of these Lagrangian particles to be the distances a measured along z. Assume that the particle having the Lagrangian coordinate a crosses the shock front at the instant $\tau(a)$. Let $v_1(a)$ and $v_2(a)$ be respectively the velocities of these particles behind the shock wave and at infinity. Note that these velocities are of the same order.

Outside the vicinities of $a\sim D_0$ and $\tau\sim t_0 = D_0/v_0$, the functions $v_{1,2}(a)$ and $v_{1,2}(\tau)$ are monotonically decreasing functions of a and τ. Here and elsewhere $D_0 = s_0^{1/2}$ is the characteristic initial dimension of the striking particle and s_0 is the particle cross-section area at the initial instant of time. For $a\sim D_0$ and $\tau\sim t_0$ we have $v_{1,2}\sim v_0$. We call this the initial stage (stage I). Two shock waves exist in the initial stage, one propagating through the particle and the other through the target. The substances spread in lateral relaxation waves that form adjacent jets of particle and target material. After the shock wave propagates through the particle, it emerges on its rear side. All the particle material then expands in rarefaction waves.

Figure 1 shows how the flow evolves in time. Figure 1a shows the initial configuration: the striking particle and the instant of contact with the target surface. The spatial dimensions are normalized to the initial particle dimension D_0, and the pressures to the characteristic pressure $\rho_t v_0^2$. For simplicity, the pressure axis in Fig. 1b is displaced to the right from the point $x = 0$. The initial-velocity vector $\mathbf{v}_0$ makes an angle α with the target surface. All the following numerical calculations were made for the characteristic velocity $v_0 = 80$ km/s of the Halley-comet dust-cloud particles impinging on the surfaces of the space instruments.

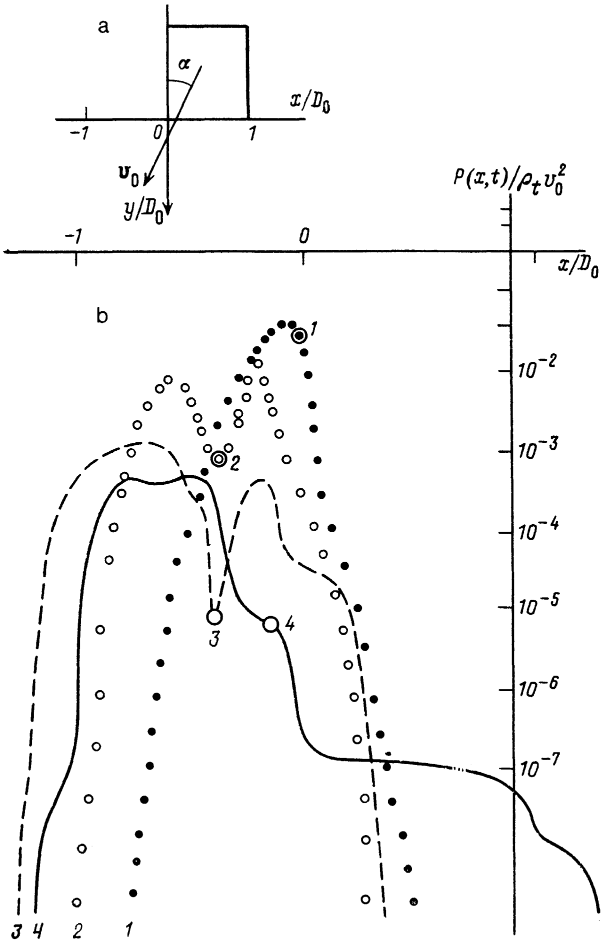

FIG. 1. a—Initial configuration: impinging dust particle at the instant of contact with the target surface. b—Evolution of contact surface and of the pressure distributions. The calculation was made for $\alpha = 45°$ and a ratio $\mu = \rho_d/\rho_t$ and initial densities ρ_d and ρ_t of the particle and target equal to 0.11. ●—Situation at $t = 0.5t_0$, ○—$t = 1.5t_0$, dashed—$t = 3.3t_0$, solid—$t = 10t_0$. Large circles *1*, *2*, *3*, and *4* show the positions of the contact surface between the particle and target materials at the corresponding times.

Figure 1b shows the evolution of the pressure distributions along the x axis for the impact geometry shown in Fig. 1a. This axis coincides at $t = 0$ with the lateral particle boundary ahead of the moving particle. During the initial interaction phases *1*, *2*, and *3* (Fig. 1b) the shock wave and the contact surface move ahead between the dust and target materials. In the later phase *4* the pressure decreases and the material expands in the relaxation wave. The contact boundary begins to move then towards the vacuum. Within times of the order of several times t_0 an inertial expansion of the particle material sets in. The spatial structure of the flow in this regime is shown in Fig. 2.

Next, as a and τ increase, the shock wave attenuates and the velocities $v_{1,2}$ decrease. The emission flare sweeps over target-material batches of constantly decreasing entropy. We call this stage II. Values $v_{1,2}\sim c_s$ are ultimately reached when the wave is damped at some a_c and τ_c. The shock wave degenerates then into a damped acoustic wave and the collision damage ceases. This is the crater-formation stage. We confine ourselves in the present paper to stages I and II.

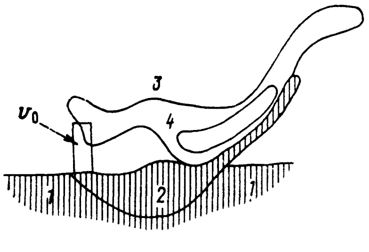

FIG. 2. Gasdynamics of the interaction of the incident particle with the target. Spatial structure of the spreading cloud at the instant $t = 16t_0$. The calculation was made for the case $\mu = 0.11$ and $\alpha = 30°$. The hatched region is occupied by the target material. Regions *1* and *2* are occupied by the unperturbed and perturbed target material, respectively. The boundary between regions *1* and *2* is a shock wave propagating through the target material. Curves *3* and *4* are isochores passing through the incident-particle material and corresponding to respective densities $0.04\rho_d$ and $0.1\rho_d$. The rectangle shows the initial position of the particle at the instant of contact with the target surface (particle with rectangular cross section with height/base ratio 3:1).

Stage III has been investigated in Refs. 12–15. It is quite clear that the computational difficulties increase as v_0/c_s increases, since computations for longer times are necessary. This calls in turn for the use of smaller cells, more accurate methods, and more computer time.

In a hypervelocity impact, when $v_0 \gg c_s$ holds, stage II turns out to be approximately self-similar. For a high-speed impact with v_0 not much larger than c_s, the boundaries of stages I, II, and III overlap. In the self-similar region the emitted target material has a power-law distribution which will be discussed below. By the time τ the expansion of the target-material batches that passed through the shock wave at $t \ll \tau$ is already inertial. The distribution function f for these batches of matter accordingly reaches its asymptotic values. Material passing through the shock wave at $t \approx \tau$ is in some intermediate state, during which the dynamic expansion becomes inertial. The function $f(\mathbf{v}, t)$ goes then through its formation stage in this portion of material.

As the asymptotic regime is approached, uniform expansion of the emission flare sets in, a velocity distribution linear in the coordinates is established, the pressure gradients decrease gradually, and the matter no longer accelerates. The flow becomes supersonic and subsequently hypersonic. The densities do not change with time if they are normalized to t^2 in planar geometry or to t^3 in cylindrical geometry. In the inertial regime, the spatial coordinates of the Lagrangian particles are given by $\mathbf{r} = \mathbf{v}t$, where $\mathbf{v}$ is independent of t. We therefore have $\partial/\partial r \propto \partial/\partial v$ and the spatial distribution of the density $\rho = \rho(\mathbf{r}, t)$ becomes similar to the distribution (2.1) of the mass in phase space (i.e., in velocity space or in hodograph space). Asymptotically the function $f(\mathbf{v}, t)$ no longer depends on time.[2)]

3. NUMERICAL METHOD

Before reporting the computed distribution functions, we describe the computation method. In our set of two-dimensional gasdynamic computations we varied a number of parameters to investigate their effects on the energy and angular distributions of the material in the flare. The calculations were performed first for a striker and target of aluminum. We note that the equation of state of aluminum is quite close to that of silicon and silicon oxide. Silicates are of interest for calculations of the results of bombardment by cosmic dust.

Various equations of state were used: tabulations, two-term equations of the Mie–Grüneisen type, and broadly applicable equations of state based on the latter. The computation results were compared with each other. A set of calculations with the equation of state of an ideal gas having different adiabatic exponents γ was performed to estimate the influence of the "rigidity" of the equation of state on the flare structure. The striker shape was also varied. The shape of a flare dust speck produced by a round striker with length-to-width ratio near unity and with the usual values of the adiabatic exponent ($\gamma = (\partial \ln p/\partial \ln \rho)_s = 1.7–3$) near the shock adiabat depends mainly on the parameters μ and α. Note that the the choice in the "Vega" experiments was $\alpha = 50°$ for the PUMA-1 instrument and $\alpha = 30°$ for PUMA-2 (Vega-2).

We confine ourselves here to an analysis of the case $\mu < 1$. This case is of interest for the PUMA-1, 2 experiments, since the value $\rho_t = 10.5$ (silver) or 19.3 (gold) is larger then the ρ_d values 0.2–1 for specks of organic matter, 2–3 for silicate, and 4–7 for those of triolite (the densities here and below are in g/cm^3). The calculations reported here were made by the familiar "particle-in-cell" method, with approximate 70×70 grids. Approximately 6×18, 10×10, or 18×6 grid cells were used for the striker. The target as a rule occupied one-third of the computation region. The grids were made coarser and rezoned when necessary. Up to 50 000 particles were used in the computations. From one to three thousand steps in time were calculated. A NORD-50 computer was used for the most part.

In the "particle-in-cell" methods it is easy to separate the contact boundaries between substances and track the Lagrangian particles. Note that the computations accurately conserved the entropy behind the shock waves along the Lagrangian-particle trajectories.

To conclude this section, we assess the influence of three-dimensional ($3D$) effects. Much attention has been paid to this question, and quite definite conclusions can be drawn at present. A distinctly oblique impact is a three-dimensional phenomenon. Technical memory and operating-time limitations of the available computers, however, made $3D$ computations impossible. The strategy resorted to was based on comparing normal impacts in planar ($2D_p$) and cylindrical (axisymmetric, $2D_a$) geometries. Incidentally, at $\mu = 0$ an oblique $3D$ impact can also be calculated in $2D_a$ geometry. In fact, the motion is then resolved into a drift along the target surface and a normal impact. A painstaking comparison has shown that three-dimensionality does not lead to essential changes. The expansion velocities are somewhat lowered, since the energy is distributed over a larger number of degrees of freedom. We conclude thus that computations in $2D_p$ geometry simulate the $3D$ situation satisfactorily.

To prevent misunderstandings, we emphasize that we are dealing with a comparison of the velocity distributions in the first batches of expanding material from the striking particle and the leading material from the target of approximately the same mass. The succeeding batches of the target mass have different asymptotic expansion velocities in the $2D_p$ and $3D$ cases, owing to the different laws governing the shock-wave damping. We emphasize in addition that we re-

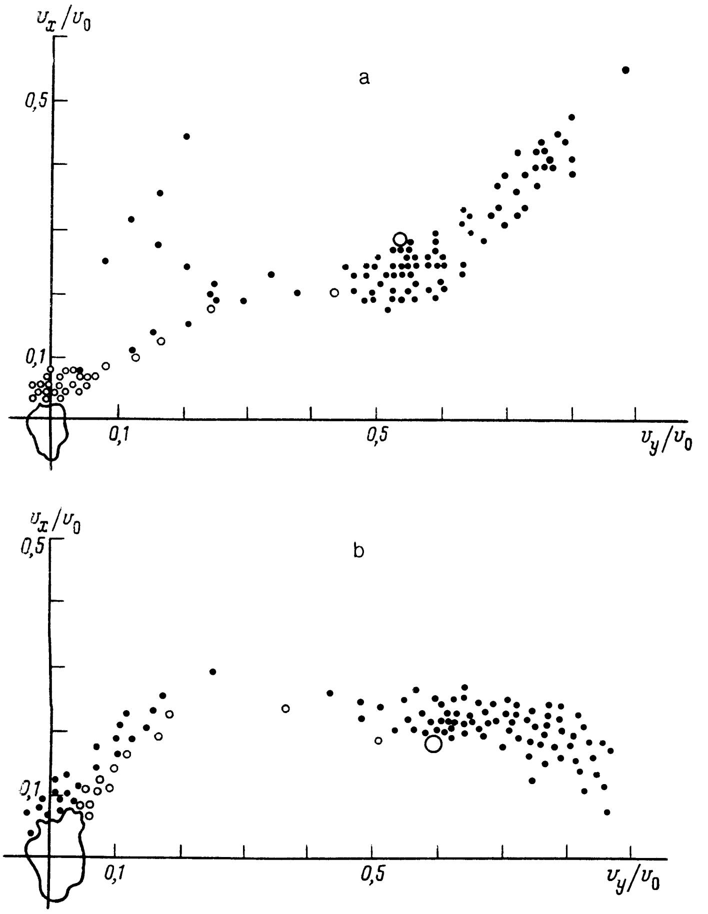

FIG. 3. *a*—Example of phase diagram in the case $\alpha = 30°$, $\mu = 0.11$. Dust material—●, target material—O. The incident particle has a square cross section. The distributions are shown for the instant $t = 10t_0$. The large circle marks the position of the mass center of the incident particle, *b*—Example of phase diagram in the case $\alpha = 30°$, $\mu = 0.37$.

fer here just to expansion velocities. Other variables, such as the density or pressure, vary differently with time at large expansions and therefore differ greatly in the $2D_p$ and $3D$ cases.

4. RESULTS OF DISTRIBUTION-FUNCTION COMPUTATIONS

Typical computed distributions $f_d(v_x,v_y,t)$ and $f_t(v_x,v_y,t)$ are shown in Fig. 3. Comparison of the distributions at the times $t = 10t_0$ and $t = 30t_0$ shows that when $t = 10t_0$ is reached the material outside the slow-motion region enclosed by the contour attains its asymptotic velocities. The distributions f_d and f_t are marked by dark and light circles, respectively. The markers are crowded in regions of increased density. One dark marker contains a dust-mass element equal to $0.01m_d$, while a light marker correspond to $0.04m_d$ (the mass-measurement unit is thus the particle mass m_d). The area enclosed by the contour contains so many light markers that they merge into one continuous spot. The lower part of the region enclosed by the contour, with $v_x < 0$, pertains to the material behind the shock wave, which continues to move into the interior of the target at the instant represented by the diagram. The contour contains a target mass amounting to $170m_d$ for the calculation shown in Fig. 3 and $77m_d$ for Fig. 3b. A two-part equation of the Mie–Grüneisen type was used for these calculations.

For $\mu < 1$ the particle material is emitted with higher velocity than the target material. This is seen from Fig. 4, which shows two density distributions along the flow-symmetry axis at the initial instant and somewhat later, respectively.

The matter distribution in the normal component of the velocity is given by the function

$$\varphi_{d,p}(v_x,t)=\frac{dm}{m_d\,dv_x}=\int\limits_{-\infty}^{+\infty} f(v_x,v_y,t)\,dv_y,\qquad \varphi(v_x)=\varphi(v_x,t=\infty). \tag{4.1}$$

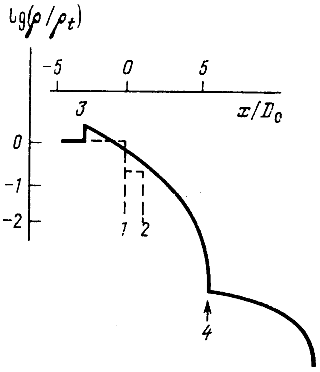

FIG. 4. Density distribution along the flow symmetry axis at $t = 0$ (dashed lines) and $t = 100t_0$ (solid). The case considered is that of normal impact of a particle of square cross section and having $\mu = 0.19$. *1*—Initial position of contact surface between the particle and the target, *2*—trailing edge of the particle at $t = 0$, *3*—position of damped shock wave traveling into the interior of the target material, *4*—contact surface at $t = 100t_0$.

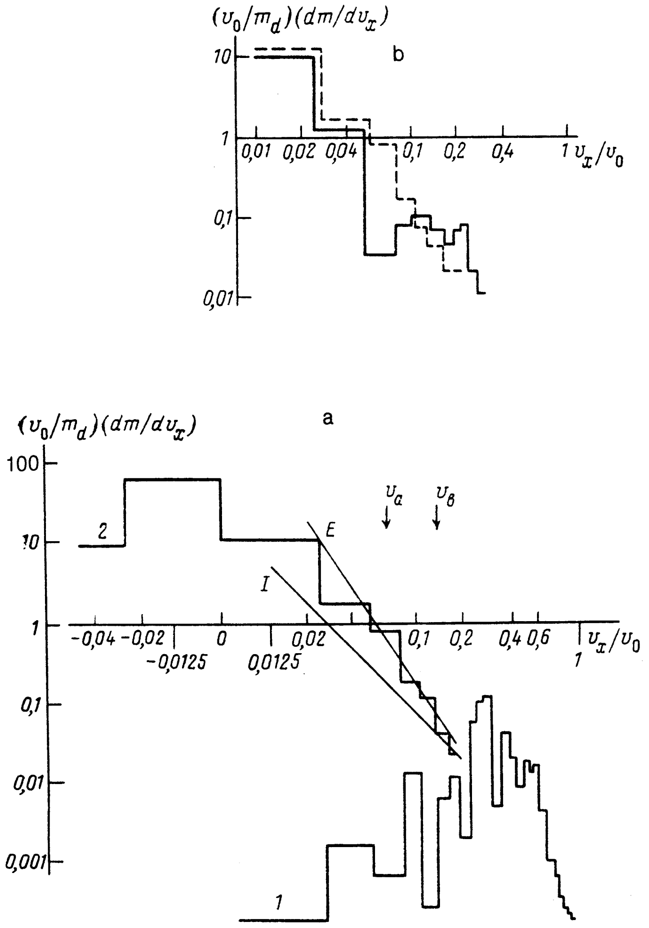

FIG. 5. a—Mass distribution over the normal velocity component v_x. Distributions *1* and *2* correspond to the dust particle and target. b—Examples of $\varphi_t(v_x)$ distributions. Case with $\alpha = 30°$, distribution *1*—solid line, $\mu = 0.37$, *2*—(dashed line), $\mu = 0.11$.

The φ_t distributions for the target material are similar. The calculation results are shown in Figs. 5a and 5b as step distributions with spacing $\Delta v_x/v_0 = 0.025$. The functions φ are obtained from the f distributions of Figs. 3a and 3b by integrating (4.1). Figure 5a shows the calculation results for $\alpha = 30°$ and $\mu = 0.11$. The distribution is shown for $t = 10t_0$. The characteristic velocities v_a and v_b for the target material and for the integrals of the energy E and of the momentum will be given later. Figure 5b shows the $\varphi_t(v_x,t)$ distributions for $t = 10t_0$.

An examination of the results shows the following. The distributions φ, and hence also the distributions f (recall that the latter is the mass distribution in velocity) consist of three sections as function of velocity (see Fig. 5). These sections are formed not simultaneously but in a succession corresponding the stages I, II, and III described in Sec. 2. The distributions of Figs. 5a and 5b correspond to rather late times, after all these sections are formed. In the high-velocity section formed during stage I the matter spreads at rates $\sim v_0$. A study of the mass distribution in velocity shows that this velocity section contains the bulk of the striking-particle material and a mass $\sim m_d$ of the target material.

Approximately self-similar power-law sections with velocities $c_s/v_0 \ll v/v_0 \ll 1$, and a section with a non-self-similar low-velocity outflow correspond to stages II and III, respectively. In the latter the material moves with velocities $\sim c_s$. This section makes the main contribution to the recoil momentum and particularly to the total ejected mass. Whereas in the high-velocity and self-similar sections the moving matter is gaseous, the low-velocity section consists of many phases. Its fast part is a gas flare and is followed first by a vapor–liquid mixture and then by a cloud of condensed particles due to the phase transition and spallation.

The calculations shown in Figs. 5a and 5b were made for an initial impact velocity $v_0 = 80$ km/sec. The slow section with velocities $v \sim c_s \sim 1$ km/s correspond to $v/v_0 \sim 0.01$. The v_x/v_0 axis scale is logarithmic above 0.0125, linear between -0.0125 and $+0.0125$, and again logarithmic below -0.0125. Such a composite scale fits both the region of slow motions in the vicinity of $v_x = 0$ and the power-law distribution at high velocities.

The low-velocity efflux is concentrated at the distribution maximum located in the vicinity of zero velocity. Material moves into the interior of the target for $v_x < 0$. The low-velocity maximum is that of the material in the vicinity of the shock wave propagating into the interior of the target (see Fig. 5), and of the undisturbed target material. The distribution function does not become infinite at $v_x = 0$ because the target mass M_t is finite in our calculation. In Figs. 3a and 3b the low-velocity maximum of the distribution function corresponds to the slow-motion region enclosed by the contour.

A strictly self-similar power-law section exists if $v_0 c_s = \infty$ and the equation of state of the target material is that of an ideal gas with an adiabatic exponent γ. The corresponding flow is generated by a "short impact" (Refs. 16, 18, 19). Generalizations to the case of more general equations of state are also possible. Thus, this question was investigated in Ref. 18 for the case $n = 1$, when the shock front is planar. The values $n = 2$ and 3 correspond respectively to filamentary and pointlike impacts that generate respectively planar and axisymmetric flows.

At $v_0/c_s \sim 100$ the pressure behind the shock wave ranges in the power-law interval from several hundred to several Mbar. In this case the adiabatic index satisfies $\gamma = (d \ln p/d \ln \rho) = 1.7$–$3$ in the vicinity of the shock adiabat and depends on the pressure. Real equations of state do not in general accord with self-similar motions. Numerical calculations[19] show, however, that for real equations of state the shock wave has a nearly power-law motion with a slowly varying exponent, and the profiles of the hydrodynamic variables are close to self-similar. A real solution is thus not exactly power-law.

We make one more remark concerning the self-similarity exponent δ. In the self-similar problem the functions $p/\dot{R}^2, \rho$, and $\mathbf{v}/\dot{R}$, are stationary in the coordinates $x/R, y/R$ and $r/R, z/R$, respectively, in planar and axisymmetric geometry. Here $R = R(0, t)$ and $R(\theta, t)$ are the front coordinates of the shock wave propagating into the interior of the target material, θ is the angle measured from the inward normal to the target surface, and

$$R(\theta, t) = \chi(\theta) R(0, t), \quad R(0, t) \sim t^{\delta},$$

where the time is measured from the instant of the short impact and $\delta = \delta(n, \gamma)$. Putting

$$\rho_t R^n = m(t), \quad \dot{R} = v(t),$$

recognizing that $R\sim t^{\delta}$, eliminating t, and taking into account that the velocity of the material flowing into the shock waves is of the order of that of the shock wave itself and of the order of the asymptotic expulsion velocity of this batch of material, we obtain the power-law distribution

$$\frac{dm}{dv}=-A\frac{n\delta}{1-\delta}\frac{m_d}{v_0}\left(\frac{v_0}{v}\right)^{\beta},$$

$$\beta=\beta(n,\delta)=\frac{(n-1)\delta+1}{1-\delta},\qquad A\approx 1.$$

The energy and momentum integrals for a power-law distributions are respectively

$$E=\frac{mv^2}{2}\sim v^{3-\beta},\qquad E=\rho_t R^n \dot{R}^2\sim\frac{1}{t^{(n+2)(\delta_E-\delta)}},\qquad \delta_E=\frac{2}{n+2}.$$

$$I=mv\sim\frac{1}{v^{\beta-2}},\qquad I=\rho_t R^n \dot{R}\sim t^{(n+1)(\delta-\delta_I)},\qquad \delta_I=\frac{1}{n+1}.$$

It is known[16,18] that $\delta_I<\delta<\delta_E$ for an ideal gas. It follows that $\beta_I<\beta<\beta_E$, where $\beta_E=\beta_E(n,\delta)=3$ and $\beta_I=\beta_I(n,\delta)=2$ is independent of n and γ. Figure 5a shows straight plots of E and I with respective slopes β_E and β_I. The $\varphi(v_x)$ distribution on the self-similar section evidently lies between two limiting power-law distributions.

Consider now the distribution-function section 1 corresponding to the fastest part of the emission flare. We are interested in the expansion rates of the materials of the impinging particle and the target, and also in how these velocities depend on the main parameters of the problem—the density ratio μ and the angle α. Calculation examples that illustrate the dependence of the distribution functions f and φ on the parameter μ are shown in Figs. 3, 4, and 5. The average spreading rates are also of interest. Their calculation for the striking-particle material is given by

$$\langle v_x\rangle=\frac{1}{m_d}\iint\rho v_x\,dx\,dy$$

$$\langle\Delta v_x\rangle=[\langle(v_x-\langle v_x\rangle)^2\rangle]^{1/2},$$

$$\langle(v_x-\langle v_x\rangle)^2\rangle=\frac{1}{m_d}\iint\rho(v_x-\langle v_x\rangle)^2\,dx\,dy.$$

In these equations ρ stands only for the density of the particle material. The calculation results are given in Table I.

The characteristic velocities for the fastest parts of the striking-particle material were obtained differently. Namely, we calculated a function $m(v)$ defined as

$$m(v)=m_d\int_v^{\infty}\varphi(v_x)\,dv_x,$$

followed by finding velocities v_a and v_b such that

$$m(v_a)=3m_d,\qquad m(v_b)=0{,}3m_d.$$

TABLE I. Asymptotic values of characteristic spreading velocities of the incident-particle material $\langle v_x\rangle/v_0$ and $\langle\Delta v_x\rangle/v_0$, percent.

α	μ		
	0,037	0,11	0,37
60°	–	29(21)	15(24)
45°	–	32(14)	–
30°	41(19)	35(15)	18(5)

Note. The variance is given in the parentheses.

TABLE II. Characteristic spreading velocities of the target material v_a/v_0 and v_b/v_0 (in parentheses), percent. Determination of the velocities v_a/v_b.*

α	μ	
	0,11	0,37
60°	6(24)	9(50)
45°	6(19)	–
30°	4(12)	4(19)

*See the text and Fig. 5a.

These velocities are shown by arrows in Fig. 5a. The dependence of v_a and v_b on μ and α is given in Table II.

The calculations were confined to the case $\mu<1$. In this case the particle does not "bury itself" deeply in the target and the characteristic spreading rates v_{hd} of the particle material exceed those (v_{bt}) of the target material. This is seen from Figs. 2–5 and from a comparison of the data in Tables I and II. Analysis of the tables shows that for fixed α and decreasing μ the velocities v_{hd} increase while v_{ht} decrease, owing to the decrease of energy transfer to the target. The latter is seen from a comparison of Figs. 3a and 3b. Superposition of the distributions in Figs. 3a and 3b shows clearly that as μ decreases the distribution f_d shifts towards higher velocities while the distribution f_t contracts and shifts towards lower velocities. The same is shown by comparison of distributions 1 and 2 of Fig. 5b. The distribution 2 corresponds to smaller μ and has a less pronounced tail of the high-velocity distribution φ_t.

At fixed μ and decreasing α less energy is transferred to the targets and the velocities v_{ht} also decrease. This is seen from an analysis of Table II.

We conclude by formulating briefly the main deductions. We have investigated by numerical methods the physics of the interaction between an incident hyperfast dust particle and a target. The calculation was by the particle-in-cell method. We used in the main a semi-phenomenological equation of state based on the Mie–Grüneisen approximation. We tracked the evolution of the flow up to the late times at which the emitted plasma flare produced by the impact reaches its asymptotic spreading regime. The dependence of the complicated form of the flare on the parameters of the problem was investigated.

[1)] In the numerical calculations M_t actually denotes the target-material mass in the computation region.

[2)] For inertial spreading of a sphere see Ref. 16, and for that of a gas ellipsoid see Ref. 17 and the citations therein.

[1] Yu. G. Malama, *Numerical simulation of ionization phenomena in high-velocity impact.* Preprint No. 725, Inst. of Space Research, USSR Academy of Sciences, 1982.

[2] R. Z. Sagdeev, S. I. Anisimov, S. B. Zhitenev *et al.*, Dokl. Akad. Nauk SSSR **279**, 613 (1984) [Sov. Phys. Dokl. **29**, 958 (1984)].

[3] I. N. Slivkov, *High-Voltage Processes in Vacuum* [in Russian], Energoatomizdat, 1986.

[4] R. V. Latham, *High-voltage Vacuum Insulation: The Physical Basis*, Academic, London (1981).

[5] G. A. Mesyats and D. I. Proskurovskii, *Pulsed Electric Discharge in Vacuum* [in Russian], Nauka, Novosibirsk, 1984.

[6] J. C. Slattery, J. S. Fürchtenicht, and D. O. Hansen, J. Spacecraft **3**, 1665 (1966).

[7] H. Fechtig, E. Grun, and J. Kissel, *Cosmic Dust*, Ed. by J. A. M. McDonnel, Wiley, 1978.

[8] W. Knabe and F. R. Krueger, Z. Naturforsch. **37a**, 1335 (1982).

[9] A. I. Akishin, V. P. Kiryukhin, L. S. Novikov, and I. N. Slivkov, Zh. Tekh. Fiz. **54**, 179 (1984) [Soviet Phys. Tech. Phys. **29**, 102 (1984)].

[10] Venus—Halley Mission—Lois-Jean, GAP (1985).

[11] J. Kissel, R. Z. Sagdeev, J. L. Bertaux *et al.*, Nature 321, 280 (1986).

[12] S. I. Anisimov, A. V. Bushman, G. I. Kanel' *et al.*, Pis'ma Zh. Eksp. Teor. Fiz. **39**, 9 (1984) [JETP Lett. **39**, 8 (1984)].

[13] S. I. Anisimov, B. A. Demidov, L. I. Rudakov *et al.*, *ibid.* **41**, 455 (1985) [**41**, 554 (1985)].

[14] V. A. Agureikin, S. I. Anisimov, A. V. Bushman *et al.*, Teplofiz. Vys. Temp. **22**, 964 (1984).

[15] S. I. Anisimov, V. P. Karyagin, V. A. Kudryashov *et al.*, Pisma Zh. Eksp. Teor. Fiz. **44**, 477 (1986) [JETP Lett. **44**, 615 (1986)].

[16] Ya. B. Zel'dovich and Yu. P. Raizer, *Physics of Shock Waves and High-Temperature Gasdynamic Phenomena*, Academic, 1967.

[17] S. I. Anisimov and N. A. Inogamov, Pis'ma Zh. Eksp. Teor. Fiz. **20**, 174 (1974) [JETP Lett. **20**, 74 (1974)].

[18] S. I. Anisimov and V. A. Kravchenko, Z. Naturforsch. **40**, 8 (1985).

[19] S. I. Anisimov and S. A. Lifshitz, Preprint, Inst. Chem Phys. and Inst. Tech. Phys. USSR,. Chernogolovka, 1989.

Translated by J. G. Adashko